Ethylenediamine Addition Improves Performance and Suppresses Phase Instabilities in Mixed-Halide Perovskites

*Margherita Taddei,[1] Joel A. Smith,[2] Benjamin M. Gallant,[2] Suer Zhou,[2] Robert J. E. Westbrook,[1] Yangwei Shi,[1] Jian Wang,[1] James N. Drysdale,[2] Declan P. McCarthy,[3] Stephen Barlow,[3] Seth R. Marder,[3,4] Henry J. Snaith[2] and David S. Ginger[1]**

AUTHOR ADDRESS**:** Department of Chemistry, University of Washington, Seattle, WA, 98195, USA

AUTHOR INFORMATION

1 Department of Chemistry, University of Washington, Seattle, WA, 98195, USA

2 Department of Physics, University of Oxford, Oxford, OX1 3PU, U.K.

3 Renewable and Sustainable Energy Institute, University of Colorado Boulder, Boulder, CO, 80303, USA

4 Department of Chemical and Biological Engineering and Department of Chemistry, University of Colorado Boulder, Boulder CO, 80303, USA

* Corresponding author: dginger@uw.edu

ABSTRACT:

We show that adding ethylenediamine (EDA) to perovskite precursor solution improves the photovoltaic device performance and material stability of high-bromide-content, methylammonium-free, formamidinium cesium lead halide perovskites $FA_{1-x}Cs_xPb(I_{1-y}Br_y)_3$ which are currently of interest for perovskite-on-Si tandem solar cells. Using spectroscopy and hyperspectral microscopy, we show that the additive improves film homogeneity and suppresses the phase instability that is ubiquitous in high-Br perovskite formulations, producing films that remain stable for over 100 days in ambient conditions. With the addition of 1 mol% EDA we demonstrate 1.69 eV-gap perovskite single-junction p-i-n devices with a V_{OC} of 1.22 V, and a champion maximum power point tracked power conversion efficiency of 18.8%, comparable to the best reported methylammonium-free perovskites. Using nuclear magnetic resonance (NMR) spectroscopy and X-ray diffraction techniques, we show that EDA reacts with FA^+ in solution, rapidly and quantitatively forming imidazolinium cations. It is the presence of imidazolinium during crystallization which drives the improved perovskite thin-film properties.

TOC

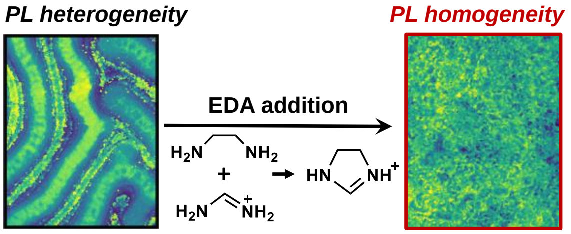

Stability > 100 days in air
V_{OC} 87% of radiative limit

Metal halide perovskites (MHPs) combine excellent semiconductor properties with the potential for scalable, low-cost manufacturing. As a result, these materials have attracted attention in optoelectronic applications ranging from photovoltaics[1], light-emitting diodes[2], and detectors[3] to elements of non-linear optics and sources of quantum light.[4] MHPs have the generic formula ABX_3 – where A (= Cs^+, methylammonium or MA^+, formamidinium or FA^+) and B (= Pb^{2+}, Sn^{2+}) are cations and X (= I^-, Br^-, Cl^-) is an anion and offer broad band gap tunability from <1.25 eV in e.g. $(FASnI_3)_{0.6}(MAPbI_3)_{0.4}$ to >2.25 eV in e.g. $CsPbBr_3$.[5,6] In photovoltaics, there is particular interest in overcoming the single-junction, detailed-balance efficiency limit using multijunction solar cells.[7,8]

The ideal bandgap for the perovskite active layer in Si-perovskite tandem solar cells is roughly 1.7 eV.[9] In order to achieve this bandgap for typical multi-cation compositions, iodide is partially replaced with bromide at the halide (X^-) site, generally using over 23% Br^-.[10] However, perovskites with high bromide/iodide ratios (>20%) usually undergo “halide segregation”, by which iodide-rich narrower bandgap regions are formed during illumination, compromising the performance and stability of the solar cell.[11,12] In recent years, due to thermal instabilities of methylammonium perovskites, compositions containing only formamidinium and cesium (FA^+/Cs^+) cations have been increasingly favored by the community.[13,14] However, these FA^+/Cs^+ compositions suffer from phase instabilities over time: the desired cubic corner-sharing (α) “black” phases separate to pure $CsPbI_3$ and $FAPbI_3$, which are 1D photoinactive, non-perovskite “yellow” phases in which the BX_6 octahedra are edge-sharing and face-sharing respectively.[15] Thus, it is necessary to find methods to limit both halide segregation and phase instability to achieve stable wide-gap compositions.

Diamines have been previously incorporated into metal halide perovskites as additives in the precursor solution.[16–19] In particular, the addition of ethylenediamine (EDA) and ethylene diammonium iodide ($EDAI_2$) has been shown to lead to the formation of "hollow" materials in certain ABI_3 ($A = MA^+, FA^+; B = Pb^{2+}, Sn^{2+}$) perovskites, whereby diammonium di-cations are incorporated into the perovskite structure, along with B^{2+} and X^- vacancies to enable steric accommodation of the EDA di-cations and balancing of the overall charge respectively.[20,21] In addition, the use of EDA via post-treatment of the surface has been reported to afford increased efficiency and stability in Pb-Sn perovskites.[22] Likewise, dimethylammonium is another bulky cation, which is too large to incorporate into many halide perovskite compositions according to the Goldschmidt tolerance factor considerations, but in some cases has been shown to increase both the bandgap, open-circuit voltage (V_{OC}), and overall performance of perovskite solar cells, despite negatively impacting the compositional heterogeneity of those films.[23–25] Motivated by these observations, we hypothesized that the addition of EDA might be beneficial for formulations close to the 1.7 eV band gap ideal for silicon-perovskite tandems. We anticipated that the addition of EDA might allow us to access a more stable compositional space, thus allowing the use of lower bromide concentrations to achieve the 1.7 eV band gap ideal for silicon-perovskite tandems.

Here, we demonstrate that incorporating EDA into a >1.68 eV bandgap $FA_{0.83}Cs_{0.17}Pb(I_{0.75}Br_{0.25})_3$ perovskite yields a significant enhancement in both chemical homogeneity and phase stability, as well as an enhancement of solar cell device performance. We show p-i-n devices with a maximum power point tracked power conversion efficiency (PCE) of 18.8% and open circuit voltage (V_{OC}) of 1.22 V with 1 mol% EDA (EDA-1) addition which is a record for this bandgap in a MA-free composition. We investigate the mechanism for these improvements using nuclear magnetic resonance (NMR) spectroscopy and X-ray diffraction

(XRD) techniques and find that EDA reacts with FA^+ in solution under the conditions employed here.

First, we investigate the effects of adding EDA to the growth solution used to deposit films of the composition $FA_{0.83}Cs_{0.17}Pb(I_{0.75}Br_{0.25})_3$, which has a bandgap close to the ideal top cell for a Si-tandem (E_g= 1.695 eV, extracted from UV-Vis of **Figure 1a**). **Figure 1a** shows that addition of 1 mol% EDA (EDA-1) as an additive in the precursor solution used to spin-coat the films causes a very slight blueshift in the absorption (E_g=1.702 eV) compared to those of the same composition without EDA (EDA-0), along with an increase in measured photoluminescence intensity. PL measurements in an integrating sphere at an intensity of 60 mW/cm^2 with a 532 nm laser indicate that the EDA-1 film has a photoluminescence quantum efficiency (PLQE) of 9.7% and the emission maximum (λ_{max}) is located at 717 nm, whereas the EDA-0 sample has a PLQE of 6.5%, with its maximum at 722 nm (**Figure S1**). **Figure 1a** also shows that the EDA-0 film has a broader PL peak, with a clear shoulder at 744 nm. We observe this shoulder growing rapidly in EDA-0 samples, even during a brief PL measurement (~timescale here 0.1s), consistent with reports of the facile segregation into I-rich and Br-rich phases for such high-bromide composition samples.[26–28]

Figure 1b shows the PL lifetime decays of the EDA-0 and EDA-1 films taken using 405 nm excitation with a pulse energy/area of ~4 nJ cm^{-2} ($N_0 = 1.8 \times 10^{14}$ cm^{-3}). Under these conditions the differences in PL dynamics between the reference and EDA-1 films is clear, with the EDA-1 film showing significantly more counts, and a longer PL lifetime. We fit the PL decays using a stretched exponential function, as we have reported previously [29,30]:

$$I(t) = A_1 e^{-\left(\frac{t}{\tau_c}\right)^{\beta}} \tag{1}$$

We use the stretched exponential to account phenomenologically for distributions of PL lifetimes that carriers excited at different lateral and vertical positions in the film may experience due to sample heterogeneity. The stretched exponential fits for the reference and EDA-1 films give τ_c and beta values of τ_c =0.6 ns, and β =0.17 for the reference film, and τ_c =301.5 ns and β =0.49 for the EDA-1 films (see **Table S1**). The stretching exponent β is indicative of the width of the lifetime distribution in an ensemble sample, with a β=1 recovering a perfectly homogeneous distribution of single-exponential emitters. Thus, the higher β value of the EDA-1 film (0.49) compared to that of the EDA-0 film (0.17) indicates a narrower distribution of emissive states, with the longer average lifetime $\tau_{stretch}$ calculated via:

$$\tau_{stretch} = \frac{\tau_c}{\beta}\Gamma\left(\frac{1}{\beta}\right) \tag{2}$$

of 627 ns for the EDA-1 film compared to 411 ns for the EDA-0 film indicating a lower distribution of non-radiative recombination pathways in the EDA-1 film.

Next, we monitor the phase stability of unencapsulated films over time whilst storing them in ambient air, in the dark, at room temperature (ISOS D-1 conditions).[31] **Figure 1c** shows the EDA-0 films rapidly (~days to weeks) revert to non-corner sharing phases in ambient conditions, as previously reported,[15] whereas the EDA-1 film is still predominantly in the desired photo-active black phase after 235 days. To quantify this stability, we use the UV-Vis absorbance of the film at 700 nm as a proxy for the remaining pseudo-cubic perovskite. **Figure 1d** plots the resulting absorbance at 700 nm for each film (full UV-Vis spectra are shown in **Figure S2**). As is typical, the EDA-0 film shows a rapid, steep drop in optical density to less than 20% of the initial value after 25 days. In contrast, the EDA-1 maintains 96% of its initial absorbance after 100 days in ambient. To characterize the phases formed during aging, we acquired XRD patterns of fresh films and after 100 days of aging in the same ambient conditions. In **Figure 1e** (full XRD patterns shown in **Figure S3**) the EDA-0 film shows the formation of several decomposition products including

$FAPbX_3$ polytype phases, orthorhombic δ-$CsPbX_3$,[32] and peaks consistent with a proposed $CsPb_2I_4Br$ phase (**Figure S4**).[33] In contrast, EDA-1 shows no additional phases detectable by XRD after 100 days of aging. The stability was also tested under a more accelerated condition with ambient light and air flow where we note that stability was further enhanced with 10 mol% EDA (EDA-10), shown in **Figure S5**.

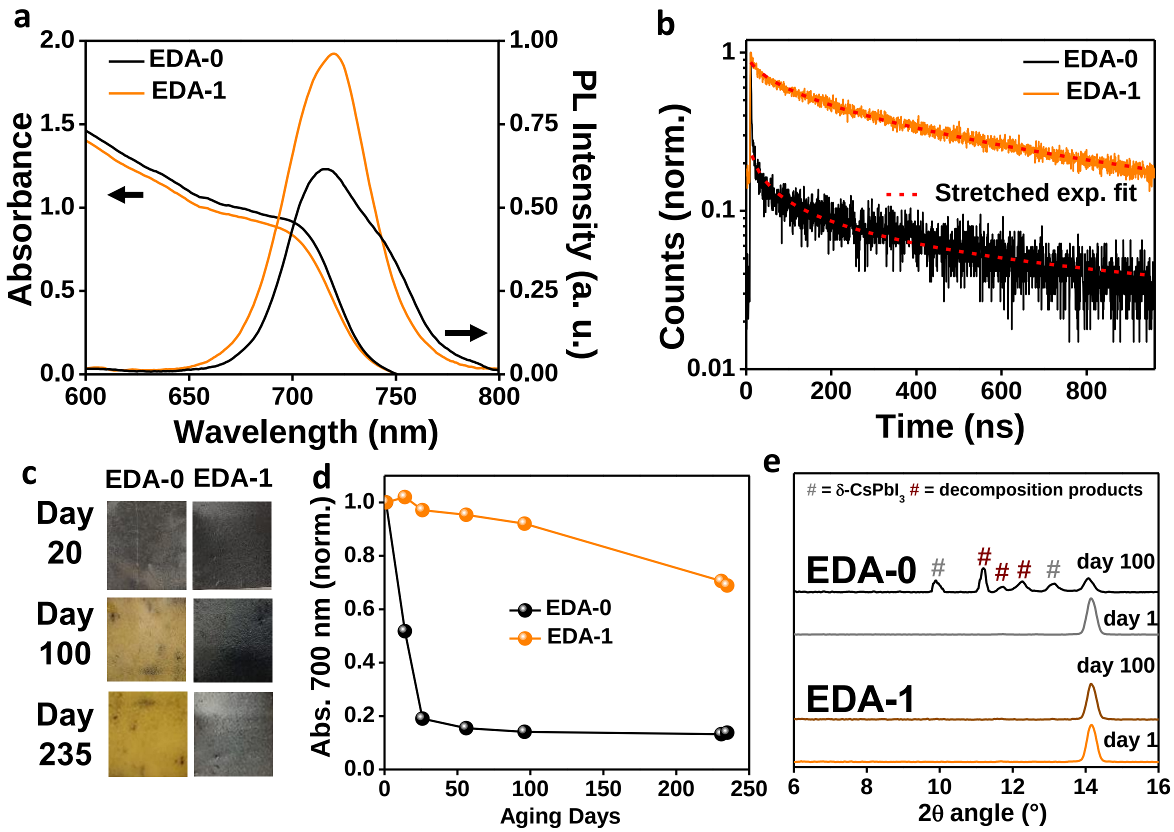

Figure 1: **Material characterization and phase stability**. *(a) UV-Vis spectra and normalized PL emission from films of* $FA_{0.83}Cs_{0.17}Pb(I_{0.75}Br_{0.25})_3$ *without EDA (EDA-0, black) and with 1% EDA (EDA-1, orange). The PL spectra are obtained using an integrating sphere coupled with a 532 nm laser at 1 Sun fluence. (b) Time resolved photoluminescence measurements using a 405 nm laser at 1 MHz pulse frequency. The fitting (dashed red line) was done using a stretched exponential decay. (c) Visual degradation of EDA-0 and EDA-1 exposed to air for 20, 100 and 235 days.*

Samples were left unencapsulated in ambient air in the dark at an average room temperature of 19.5°C and relative humidity of 31%. (d) Absorbance from UV-Vis of EDA-0 (black) and EDA-1 (orange) at 700 nm during ambient aging. (e) XRD patterns in the $2\theta = 6°$-$16°$ region of the fresh EDA-0 (grey) and EDA-1(orange) and after 100 days of ambient aging (EDA-0: black, EDA-1: brown).

Given the promising increases in stability, PLQY, and PL lifetime, we fabricated p-i-n solar cells using EDA as an additive, with the device architecture glass/ITO/Me-4PACz/np-Al_2O_3/perovskite/PCBM/BCP/Au, where Me-4PACz is a carbazole-based self-assembled monolayer (SAM) hole extraction layer ([4-(3,6-dimethyl-9H-carbazol-9-yl)butyl]phosphonic acid), np-Al_2O_3 is a dilute nanoparticle alumina layer employed to improve the perovskite solution wetting, PCBM ([6,6]-phenyl-C61-butyric acid methyl ester) is the electron extraction layer, and BCP (bathocuproine) rectifies the fullerene/metal junction.[34] Employing perovskite precursor solutions with a range of EDA additions from 0 - 3 mol% had a marked effect on the device performance measured under standard conditions (full details given in the Methods). **Figure 2a** shows stabilized maximum power point (MPP) efficiencies of the resulting devices (0.25 cm^2 active area), with the MPP shown for more representative performance comparison.[35] The full current-voltage (JV) performance metrics – power conversion efficiency (PCE), short-circuit current density (J_{SC}), fill factor (FF) and V_{OC} – are shown in **Figure S6.** The V_{OC} increases steadily with EDA addition over the concentration series, which we propose could be due to a combination of passivation and/or blueshift effects with the additive. Both J_{SC} and FF reach a maximum at 1% EDA, with a particularly severe decline in J_{SC} above this optimum value probably related to the lower relative intensity and blueshift of the band edge with additional EDA.

Figure 2b shows the *JV* results from the best EDA-1 device with a maximum PCE of 19.07%, V_{OC} of 1.22V, J_{SC} of 19.1 mA/cm^2, and FF of 82%, with little observable hysteresis. We verified the measured J_{SC} using external quantum efficiency (EQE) measurements, with the integrated current over the spectral range in perfect agreement with the *JV*-determined J_{SC} (**Figure S7)**. The results for the EDA-1 device were compared to the literature on MA-free wide-gap compositions (**Table S2**).

Our champion 19.07% PCE for a 1.685 eV bandgap composition compares favorably to other reports (**Figure S8**), in particular the high V_{OC} of 1.22 V, shown in **Figure 2c**. Additionally, in **Figure S9** we show the performance for larger 1 cm^2 devices fabricated in the same batches and on the same device substrates as the small area cells. Notably, EDA-1 devices show significantly higher average and champion efficiencies compared to without the additive. In **Figure 2d** we show the *JV* curve and stabilized MPP tracking of the champion EDA-1 large area device (16.7% MPP PCE). We attribute this improvement to an improvement in the spin-coated film morphology over larger areas, which is crucial for any precursor solution to be suitable for scale-up and led us to investigate film morphology further.

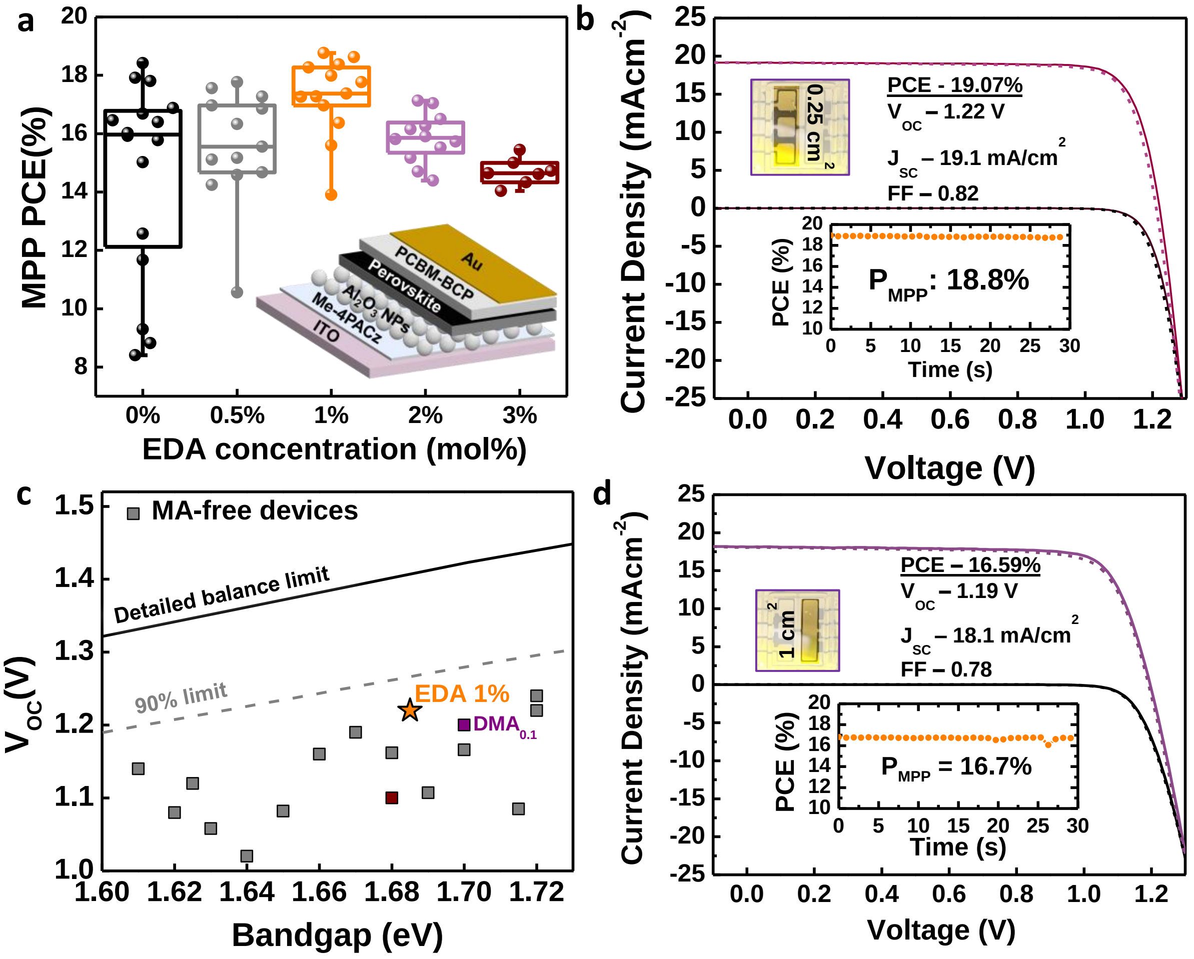

*F**igure 2:*** **Photovoltaic device results**. *(a) Inset: Schematic of the perovskite solar cell device architecture we employ. Main: efficiencies of solar cells made with 0-3 mol% EDA as an additive to the perovskite solution after 30 s of operation. (b) JV curves of the EDA-1 device under 1 sun simulated solar illumination, recorded in forward (from short to open circuit) and reverse (from open to short circuit) bias. The inset tracks the PCE over 30 s of MPP-tracked device operation. Inset picture shows the device pixel area (0.25 cm^2). (c) Open circuit voltage (V_{OC}) results from the literature of wide gap devices made with $FA_{1-y}Cs_yPb(I_{1-x}Br_x)_3$ compositions. The additive used in the best performing devices are noted next to the V_{OC} values. Purple data are from Ref.[23] using DMA$^+$. Brown points are from Ref.[36] using the same perovskite composition as this work*

($FA_{0.83}Cs_{0.17}Pb(I_{0.75}Br_{0.25})_3$. All references used in parts (c) are given in ***Table S2****. (d) JV curves of the EDA-1 large area champion device under 1 sun simulated solar illumination, recorded in forward (from short to open circuit) and reverse (from open to short circuit) bias. The inset tracks the PCE over 30 s of MPP-tracked device operation. Inset picture shows the device pixel area (1 cm^2).*

To better understand the origins of the improved stability, PL, and device performance, we explored how the PL varied on the microscale using hyperspectral microscopy (**Figure 3a and 3c**). A hyperspectral microscope obtains a PL spectrum at every pixel with high spatial resolution (for setup details see methods section) and has been used to spatially resolve heterogeneity in perovskites[37–39] and other semiconductors. **Figure 3b and 3d** plot summaries of the hyperspectral data cubes showing the wavelength-integrated total PL intensity, as well as the peak emission wavelength at every point in the sample. These measurements show that the that the EDA-1 processed films are significantly more homogeneous in both PL intensity, and PL peak wavelength than the EDA-0 films. The luminescent regions in EDA-0 are more red-shifted in accordance with them being more iodide-rich - narrower gap - regions into which charge carriers are funneled and recombine radiatively with high efficiency.[11,40] Generally, these microscopic results provide insight into the area-averaged spectra shown in Figure 1. Indeed, the histogram in **Figure 3b** shows the reference films exhibit a much wider distribution of local PL intensities, with many areas of the film being effectively dark. Similarly, the peak emission wavelength is also affected by the additive. Whereas the local emission peak wavelength varies between ~720 to 780 nm in the reference films, the EDA-1 films show a narrow clustering of the emission peaking around ~744 nm, consistent with the area-averaged data (**Figure 3d**). These data help explain the improved stability and device performance. The increased PLQY indicates a reduction in trap density in the EDA-1 films, facilitating larger quasi-Fermi-level splitting under illumination and therefore increased V_{OC},[41–43] and additionally the improved homogeneity could help improve V_{OC} of the EDA-1 films by reducing pinning to the low bandgap regions of the film, which is a common problem in complex semiconductors.[44,45] Moreover, it has been shown recently that compositional inhomogeneity of the perovskite phase is primary cause of phase instability in $FA_{1-x}Cs_{0.x}Pb(I_{1-y}Br_y)_3$ perovskites.[46–48] **Figure S10** shows the formation of "wrinkled" [49–52] films when using a higher precursor solution concentration (1.45 M). Even in this case, EDA-1 films show more homogeneous PL intensity and wavelength distributions compared to EDA-0. **Figure S11** also shows 10 mol% addition of EDA (EDA-10) shows homogenized PL and emission wavelength distribution in the microscale. Several studies have shown that light and oxygen induce halide segregation in mixed cation mixed halide compositions.[53,54] In **Figure S12** we show that under constant illumination, hyperspectral imaging shows that the control films are more heterogeneous than films with EDA addition. To further investigate the compositional variation between the samples, we performed scanning electron microscopy energy-dispersive X-ray analysis (SEM EDS) analysis at various points over the film surfaces for the EDA-0 and EDA-10 films. **Figure S13** shows that the EDA-0 film has greater variation in atomic composition compared to the narrowly distributed EDA-10 film.

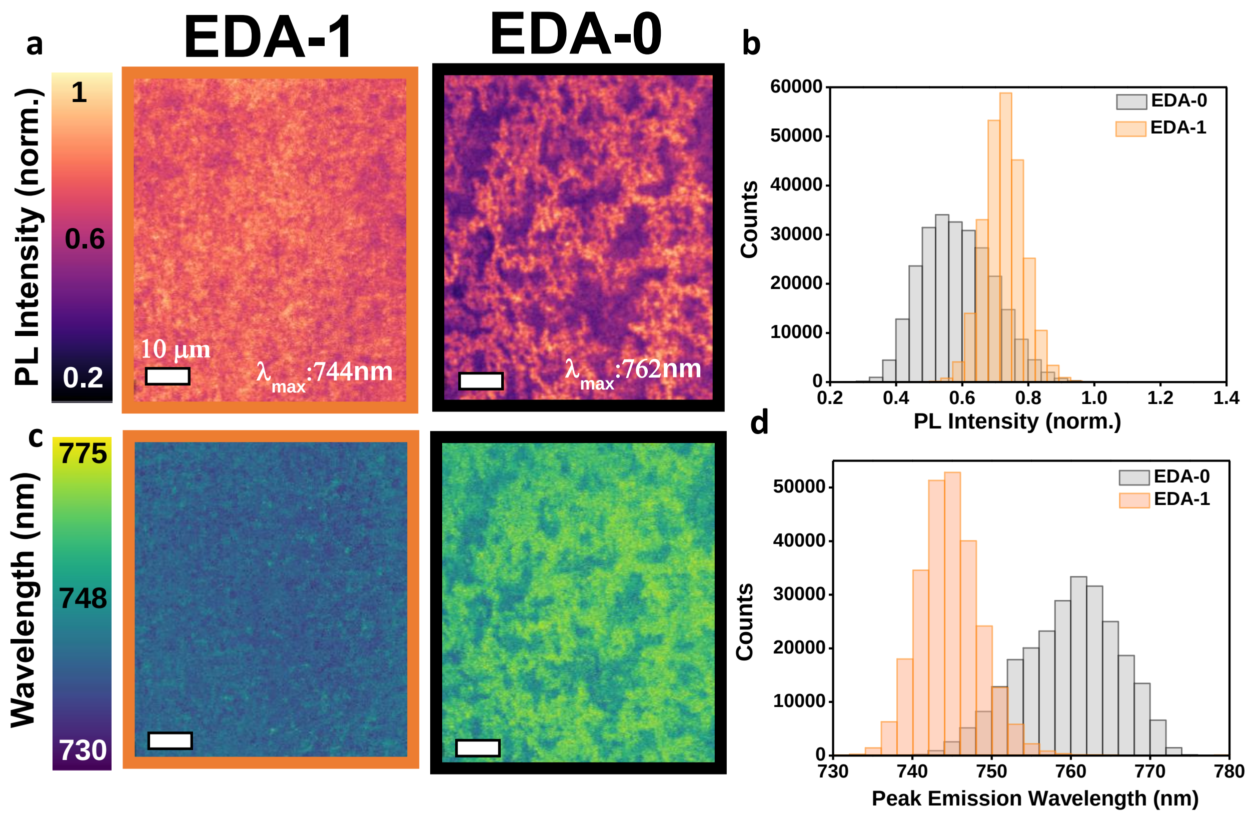

Figure 3: **Halide heterogeneity on the microscale.** *(a) Hyperspectral PL intensity map of the EDA-0 (black box) and EDA-1 (orange box). PL images are shown at the maximum emission wavelength (λ_{max}) for each sample as stated on the figure (EDA-0 λ_{max} = 762 nm, EDA-1 λ_{max} = 744 nm). Excitation was achieved with a white lamp with short pass filter at 500 nm. The emission was recorded using a 500 nm dichroic and 650 nm long pass filter. (b) Histogram of the PL intensity distribution at the maximum emission wavelength for EDA-0 (grey) and EDA-1 (orange) samples. (c) Peak emission wavelength map of the EDA-0 and EDA-1 films. (d) Histogram of the distribution of peak emission wavelengths for the EDA-0 (grey) and EDA-1 (orange) samples.*

To better understand the effects of EDA addition on film formation, we investigated the crystallization of films by blade coating solutions and acquiring *in situ* grazing-incidence wide-angle X-ray scattering (GIWAXS) measurements (described in the Methods, scheme shown in

Figure S14). For all samples (0%, 1% and 10% EDA) we identify that there exists an intermediate phase, which is a 2H polytype.[55] In the EDA-0 sample, this phase subsequently converts fully into a pseudo-cubic (3C) perovskite phase upon annealing (**Figure S15a**). However, with EDA-10 we find that in addition to the corner-sharing (α) perovskite phase, a different 2H polytype and a 4H polytype[55,56] are also formed in the fully annealed films (**Figure S15c**). For the EDA-1 sample, we detect a weak signature of a new polytype (**Figure S15f**). These results indicate that the EDA additive is altering the growth and resultant film composition at the studied concentrations.

In the SI we investigate and discuss the impact of higher EDA concentrations upon crystallization and phase behavior in thin films (**SI Note 1, Figure S16-S19, S21-S26)**. Significantly, we note that the XRD peaks from the 2H phase at a high EDA concentration (40 mol%) are a close match for a reported imidazolium lead iodide ($ImPbI_3$) 2H phase **(Figure S20)**.[57,58] We therefore investigated the possibility of larger cations forming in solution by conducting a range of NMR measurements. In **Figure 4a**, we show ^{1}H NMR spectra of our perovskite precursor materials with and without 10 mol% EDA and compare these to neat FAI and EDA, with all materials dissolved in d^{6}-DMSO (full spectra in **Figure S27)**. Unexpectedly, the addition of 10 mol% EDA does not lead to the appearance of the signals observed for neat EDA (δ 2.47, 1.23 ppm) but instead to the appearance of two new ^{1}H signals at 7.85 ppm (1H, t) and 3.62 ppm (4H, s). ^{1}H-^{1}H correlation spectroscopy (COSY) reveals off-diagonal signals demonstrating spin-spin coupling between these two new signals, indicating that they correspond to ^{1}H environments in the same molecule (**Figure 4b**). In ^{13}C NMR (**Figure S28)** signals observed in spectra acquired from EDA, FAI and perovskite solutions correspond to the expected ^{13}C environments. However, in the EDA-10 precursor solution we again observe two unexpected ^{13}C signals, and the absence of a signal corresponding to the carbon environment of neat EDA.

Significantly, ^1H-^{13}C heteronuclear single quantum correlation (HSQC) spectroscopy of the EDA-10 precursor solution (**Figure S29**) reveals that the proton giving rise to the unexpected signal at 3.62 ppm is bonded to the carbon corresponding to the signal observed at 48.6 ppm, suggesting the presence of a new alkyl carbon bonded to an electronegative atom. The proximity of the new ^1H and ^{13}C signals at 7.85 ppm and 161.9 ppm, respectively, to those corresponding to the methine environment of FA^+ suggest that the new species formed in solution also contains an amidinium group. That the ^1H signal at 3.62 ppm is shown to be both attached to an alkyl carbon and spin-spin coupled to the new ^1H methine environment strongly implies the formation of a new species in solution by direct reaction between FA^+ and EDA. The 4:1 stoichiometry of alkyl:methine ^1H signals suggests a 1:1 reaction. As the four alkyl hydrogens of EDA remain equivalent in the new species, we deduce that the symmetry of both FA^+ and EDA is retained in the new species.

Given these findings, we propose that consecutive addition-elimination reactions occur in solution leading to the formation of a secondary amidinium cation contained within a five-membered ring, 2-imidazolinium (4,5-dihydroimidazolium, $C_3H_7N_2^+$, Imn^+), and the elimination of two equivalents of volatile ammonia (inset of **Figure 4b**). We account mechanistically for this reaction in **Figure S30**. Such amine-amidinium reactions have precedent in recent perovskite literature,[59,60] and specifically this reaction is noted in early synthesis protocols for imidazolines.[61] To further support the proposed formation of Imn^+, time-of-flight secondary ion mass spectrometry (ToF-SIMS) (**Figure S31**) data shows a high intensity $C_3H_7N_2$+ mass fragment consistent with the formation of a Imn^+ in the EDA-1 and EDA-20 films.

With this reaction we can rationalize why, in our study, the EDA additive does not result in a hollow perovskite, as in previous works EDA was generally employed in acidic growth conditions and so is easily protonated. Under such conditions, or in solutions where EDA^{2+} is added directly, there is only a negligible quantity of ethylenediamine present at any time. As the diamine nucleophile is necessary to produce Imn^+ via reaction with FA^+, such conditions would effectively prevent its formation. To support this hypothesis, we verified that we do not form any polytype phases when we add the diammonium salts $EDAH_2I_2$ or $EDAH_2Br_2$ (**Figure S32**), or when we only have MA^+ rather than FA^+ in solution (**Figure S33**). The lattice volume expands in such cases, indicating EDA/EDA^+ inclusion.

While it is clear that EDA is converted to imidazolinium, typically before the film is even spin-coated, and that the resulting films are more homogenous, the exact impact of the imidazolinium remains open for further investigation. We hypothesize that the imidazolinium, and the associated 2H polytype phases, could play a variety of roles including passivating exposed interfaces, helping nucleate or template the growth of the desired perovskite phase, or even serving as a reservoir/sequestration of halide ions away from the active perovskite phase.

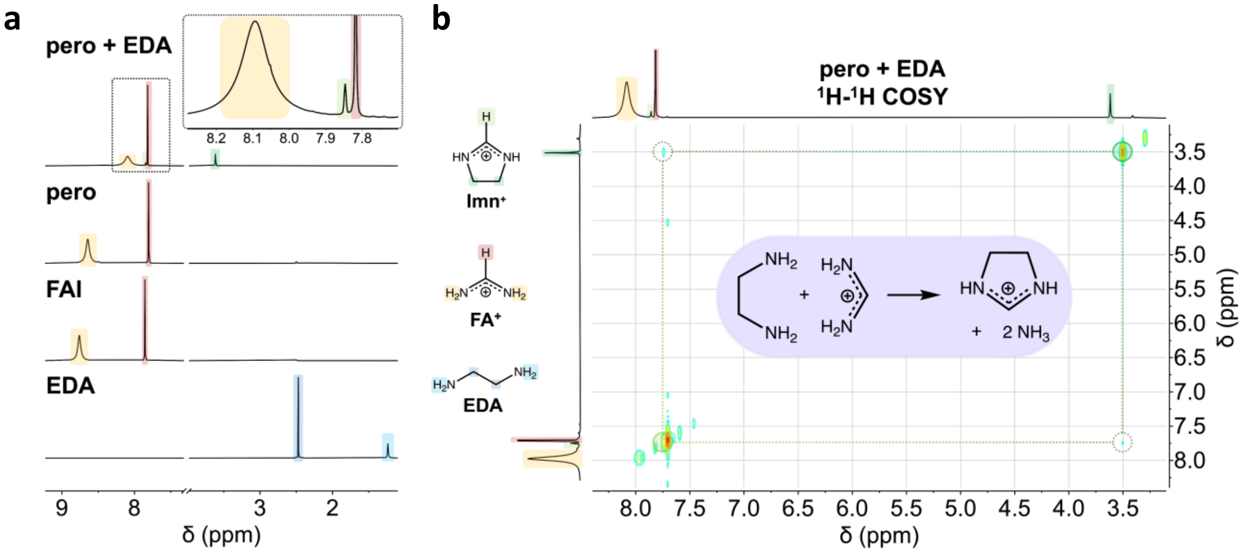

Figure 4: **Chemical Origins of EDA Effects** *(a)* ^1H *solution NMR spectra of (bottom to top) ethylenediamine (EDA), formamidinium iodide and* $(FA_{0.83}Cs_{0.17})Pb(I_{0.75}Br_{0.25})_3$ *without and with 10 mol% EDA added. (b)* ^1H-^1H *correlation spectroscopy (COSY) of* $(FA_{0.83}Cs_{0.17})Pb(I_{0.75}Br_{0.25})_3$

with 10 mol% EDA added. Off-diagonal correlation indicates corresponding ^1H *chemical environments are spin-spin coupled. All materials are dissolved in* d^6 *DMSO. The inset highlighted in purple shows the overall reaction of* FA^+ *with EDA to produce* Imn^+ *and ammonia.*

In summary, we see that EDA has a beneficial effect on the stability of MA^+-free mixed-cation mixed-halide perovskite compositions. We are able to achieve an outstanding V_{OC} and MPP-tracked PCE of 1.22 V and 18.8%, respectively, for MA^+-free devices with a bandgap of ~1.7 eV (1.69 eV), which is highly suitable for perovskite-on-Si tandem devices. We observe that EDA reacts with FA^+ in solution to form imidazolinium, which impacts the thin-film crystallization pathway and correlates with significantly improved compositional homogeneity, thin-film ambient stability and device performance. Importantly, this approach of using amine additives can be generalized to the production of other amidinium-derived compounds and may enable a range of species which are otherwise challenging to isolate. Similar approaches could be used to further engineer the surface chemistry and enhance the stability of halide perovskites.

Supporting Information

The Supporting Information is available free of charge on the ACS Publications website at DOI:XXX

Experimental methods, including thin-film synthesis, spectroscopic and microscopic characterization, device fabrication, and testing, further supporting discussion on GIWAXS and XRD data, additional references and figures (PDF).

Notes

The author declares the following competing financial interest(s): H.J.S. is a cofounder and CSO of Oxford PV Ltd.

Acknowledgements

This paper is based on work supported primarily by the Office of Naval Research (Award # N00014-20-1-2587). ToF-SIMS and part of the XRD analysis were carried out at the Molecular Analysis Facility, a National Nanotechnology Coordinated Infrastructure site at the University of Washington which is supported in part by the National Science Foundation (NNCI-1542101), the Molecular Engineering & Sciences Institute, and the Clean Energy Institute. The SEM analysis was carried out in the UW Clean Energy Institute Research Training Testbed facility. TRPL and some PL measurements were performed using the shared user facilities of UW's Molecular Engineering Materials Center, an NSF MRSEC (DMR-1719797). M.T. thanks Dan Graham at the Molecular Analysis Facility at the University of Washington for his help with ToF-SIMS data collection and analysis and Hannah Contreras for experimental help. D.S.G. acknowledges salary and infrastructure support from the Washington Research Foundation, the Alvin L. and Verla R. Kwiram endowment, and the B. Seymour Rabinovitch Endowment. S.Z. acknowledges receiving funding from the Rank Prize Funds. We acknowledge Diamond Light Source for time on beamline I07 under proposal SI30612-1 for the GIWAXS measurements and thank Saqlain Choudhary and Dr. Hadeel Hussain for assistance and Dr. Daniel Toolan and Karl-Augustin Zaininger for use of the *in situ* blade coater during these experiments.

References

(1) Correa-Baena, J.-P.; Saliba, M.; Buonassisi, T.; Grätzel, M.; Abate, A.; Tress, W.; Hagfeldt, A. Promises and Challenges of Perovskite Solar Cells. *Science* **2017**, *358* (6364), 739–744.
(2) Lin, K.; Xing, J.; Quan, L. N.; de Arquer, F. P. G.; Gong, X.; Lu, J.; Xie, L.; Zhao, W.; Zhang, D.; Yan, C.; Li, W.; Liu, X.; Lu, Y.; Kirman, J.; Sargent, E. H.; Xiong, Q.; Wei, Z. Perovskite Light-Emitting Diodes with External Quantum Efficiency Exceeding 20 per Cent. *Nature* **2018**, *562* (7726), 245–248.
(3) Basiricò, L.; Ciavatti, A.; Fraboni, B. Solution-Grown Organic and Perovskite X-Ray Detectors: A New Paradigm for the Direct Detection of Ionizing Radiation. *Advanced Materials Technologies* **2021**, *6* (1), 2000475.

(4) Muckel, F.; Guye, K. N.; Gallagher, S. M.; Liu, Y.; Ginger, D. S. Tuning Hybrid Exciton–Photon Fano Resonances in Two-Dimensional Organic–Inorganic Perovskite Thin Films. *Nano Lett.* **2021**, *21* (14), 6124–6131.

(5) Li, C.; Song, Z.; Chen, C.; Xiao, C.; Subedi, B.; Harvey, S. P.; Shrestha, N.; Subedi, K. K.; Chen, L.; Liu, D.; Li, Y.; Kim, Y.-W.; Jiang, C.; Heben, M. J.; Zhao, D.; Ellingson, R. J.; Podraza, N. J.; Al-Jassim, M.; Yan, Y. Low-Bandgap Mixed Tin–Lead Iodide Perovskites with Reduced Methylammonium for Simultaneous Enhancement of Solar Cell Efficiency and Stability. *Nat Energy* **2020**, *5* (10), 768–776.

(6) Kulbak, M.; Cahen, D.; Hodes, G. How Important Is the Organic Part of Lead Halide Perovskite Photovoltaic Cells? Efficient $CsPbBr_3$ Cells. *J. Phys. Chem. Lett.* **2015**, *6* (13), 2452–2456.

(7) McMeekin, D. P.; Sadoughi, G.; Rehman, W.; Eperon, G. E.; Saliba, M.; Horantner, M. T.; Haghighirad, A.; Sakai, N.; Korte, L.; Rech, B.; Johnston, M. B.; Herz, L. M.; Snaith, H. J. A Mixed-Cation Lead Mixed-Halide Perovskite Absorber for Tandem Solar Cells. *Science* **2016**, *351* (6269), 151–155.

(8) Leijtens, T.; Bush, K. A.; Prasanna, R.; McGehee, M. D. Opportunities and Challenges for Tandem Solar Cells Using Metal Halide Perovskite Semiconductors. *Nat Energy* **2018**, *3* (10), 828–838.

(9) Eperon, G. E.; Hörantner, M. T.; Snaith, H. J. Metal Halide Perovskite Tandem and Multiple-Junction Photovoltaics. *Nat Rev Chem* **2017**, *1* (12), 0095.

(10) Lin, Y.-H.; Sakai, N.; Da, P.; Wu, J.; Sansom, H. C.; Ramadan, A. J.; Mahesh, S.; Liu, J.; Oliver, R. D. J.; Lim, J.; Aspitarte, L.; Sharma, K.; Madhu, P. K.; Morales-Vilches, A. B.; Nayak, P. K.; Bai, S.; Gao, F.; Grovenor, C. R. M.; Johnston, M. B.; Labram, J. G.; Durrant, J. R.; Ball, J. M.; Wenger, B.; Stannowski, B.; Snaith, H. J. A Piperidinium Salt Stabilizes Efficient Metal-Halide Perovskite Solar Cells. *Science* **2020**, *369* (6499), 96–102.

(11) Motti, S. G.; Patel, J. B.; Oliver, R. D. J.; Snaith, H. J.; Johnston, M. B.; Herz, L. M. Phase Segregation in Mixed-Halide Perovskites Affects Charge-Carrier Dynamics While Preserving Mobility. *Nat Commun* **2021**, *12* (1), 6955.

(12) Wieghold, S.; Tresback, J.; Correa-Baena, J.-P.; Hartono, N. T. P.; Sun, S.; Liu, Z.; Layurova, M.; VanOrman, Z. A.; Bieber, A. S.; Thapa, J.; Lai, B.; Cai, Z.; Nienhaus, L.; Buonassisi, T. Halide Heterogeneity Affects Local Charge Carrier Dynamics in Mixed-Ion Lead Perovskite Thin Films. *Chem. Mater.* **2019**, *31* (10), 3712–3721.

(13) Juarez-Perez, E. J.; Ono, L. K.; Maeda, M.; Jiang, Y.; Hawash, Z.; Qi, Y. Photodecomposition and Thermal Decomposition in Methylammonium Halide Lead Perovskites and Inferred Design Principles to Increase Photovoltaic Device Stability. *J. Mater. Chem. A* **2018**, *6* (20), 9604–9612.

(14) Conings, B.; Drijkoningen, J.; Gauquelin, N.; Babayigit, A.; D'Haen, J.; D'Olieslaeger, L.; Ethirajan, A.; Verbeeck, J.; Manca, J.; Mosconi, E.; Angelis, F. D.; Boyen, H.-G. Intrinsic Thermal Instability of Methylammonium Lead Trihalide Perovskite. *Advanced Energy Materials* **2015**, *5* (15), 1500477.

(15) An, Y.; Hidalgo, J.; Perini, C. A. R.; Castro-Méndez, A.-F.; Vagott, J. N.; Bairley, K.; Wang, S.; Li, X.; Correa-Baena, J.-P. Structural Stability of Formamidinium- and Cesium-Based Halide Perovskites. *ACS Energy Lett.* **2021**, *6* (5), 1942–1969.

(16) Kerner, R. A.; Schloemer, T. H.; Schulz, P.; Berry, J. J.; Schwartz, J.; Sellinger, A.; Rand, B. P. Amine Additive Reactions Induced by the Soft Lewis Acidity of Pb^{2+} in Halide

Perovskites. Part II: Impacts of Amido Pb Impurities in Methylammonium Lead Triiodide Thin Films. *J. Mater. Chem. C* **2019**, *7* (18), 5244–5250.

(17) Kerner, R. A.; Schloemer, T. H.; Schulz, P.; Berry, J. J.; Schwartz, J.; Sellinger, A.; Rand, B. P. Amine Additive Reactions Induced by the Soft Lewis Acidity of Pb $^{2+}$ in Halide Perovskites. Part I: Evidence for Pb–Alkylamide Formation. *J. Mater. Chem. C* **2019**, *7* (18), 5251–5259.

(18) Wu, W.-Q.; Yang, Z.; Rudd, P. N.; Shao, Y.; Dai, X.; Wei, H.; Zhao, J.; Fang, Y.; Wang, Q.; Liu, Y.; Deng, Y.; Xiao, X.; Feng, Y.; Huang, J. Bilateral Alkylamine for Suppressing Charge Recombination and Improving Stability in Blade-Coated Perovskite Solar Cells. *Science Advances 5* (3), eaav8925.

(19) Xu, Y.; Xu, W.; Hu, Z.; Steele, J. A.; Wang, Y.; Zhang, R.; Zheng, G.; Li, X.; Wang, H.; Zhang, X.; Solano, E.; Roeffaers, M. B. J.; Uvdal, K.; Qing, J.; Zhang, W.; Gao, F. Impact of Amine Additives on Perovskite Precursor Aging: A Case Study of Light-Emitting Diodes. *J. Phys. Chem. Lett.* **2021**, *12* (25), 5836–5843.

(20) Ke, W.; Stoumpos, C. C.; Zhu, M.; Mao, L.; Spanopoulos, I.; Liu, J.; Kontsevoi, O. Y.; Chen, M.; Sarma, D.; Zhang, Y.; Wasielewski, M. R.; Kanatzidis, M. G. Enhanced Photovoltaic Performance and Stability with a New Type of Hollow 3D Perovskite {en}FASnI $_3$. *Sci. Adv.* **2017**, *3* (8), e1701293.

(21) Li, C.; Guerrero, A.; Huettner, S.; Bisquert, J. Unravelling the Role of Vacancies in Lead Halide Perovskite through Electrical Switching of Photoluminescence. *Nature Communications* **2018**, *9* (1), 5113.

(22) Hu, S.; Otsuka, K.; Murdey, R.; Nakamura, T.; Truong, M. A.; Yamada, T.; Handa, T.; Matsuda, K.; Nakano, K.; Sato, A.; Marumoto, K.; Tajima, K.; Kanemitsu, Y.; Wakamiya, A. Optimized Carrier Extraction at Interfaces for 23.6% Efficient Tin–Lead Perovskite Solar Cells. *Energy Environ. Sci.* **2022**, *15* (5), 2096–2107.

(23) Palmstrom, A. F.; Eperon, G. E.; Leijtens, T.; Prasanna, R.; Habisreutinger, S. N.; Nemeth, W.; Gaulding, E. A.; Dunfield, S. P.; Reese, M.; Nanayakkara, S.; Moot, T.; Werner, J.; Liu, J.; To, B.; Christensen, S. T.; McGehee, M. D.; van Hest, M. F. A. M.; Luther, J. M.; Berry, J. J.; Moore, D. T. Enabling Flexible All-Perovskite Tandem Solar Cells. *Joule* **2019**, *3* (9), 2193–2204.

(24) Eperon, G. E.; Stone, K. H.; Mundt, L. E.; Schloemer, T. H.; Habisreutinger, S. N.; Dunfield, S. P.; Schelhas, L. T.; Berry, J. J.; Moore, D. T. The Role of Dimethylammonium in Bandgap Modulation for Stable Halide Perovskites. *ACS Energy Lett.* **2020**, *5* (6), 1856–1864.

(25) Jariwala, S.; Kumar, R. E.; Eperon, G. E.; Shi, Y.; Fenning, D. P.; Ginger, D. S. Dimethylammonium Addition to Halide Perovskite Precursor Increases Vertical and Lateral Heterogeneity. *ACS Energy Lett.* **2022**, *7* (1), 204–210.

(26) Yoon, S. J.; Kuno, M.; Kamat, P. V. *Shift Happens* . How Halide Ion Defects Influence Photoinduced Segregation in Mixed Halide Perovskites. *ACS Energy Lett.* **2017**, *2* (7), 1507–1514.

(27) Slotcavage, D. J.; Karunadasa, H. I.; McGehee, M. D. Light-Induced Phase Segregation in Halide-Perovskite Absorbers. *ACS Energy Lett.* **2016**, *1* (6), 1199–1205.

(28) Barker, A. J.; Sadhanala, A.; Deschler, F.; Gandini, M.; Senanayak, S. P.; Pearce, P. M.; Mosconi, E.; Pearson, A. J.; Wu, Y.; Srimath Kandada, A. R.; Leijtens, T.; De Angelis, F.; Dutton, S. E.; Petrozza, A.; Friend, R. H. Defect-Assisted Photoinduced Halide

Segregation in Mixed-Halide Perovskite Thin Films. *ACS Energy Lett.* **2017**, *2* (6), 1416–1424.

(29) Oliver, R. D. J.; Caprioglio, P.; Peña-Camargo, F.; Buizza, L. R. V.; Zu, F.; Ramadan, A. J.; Motti, S. G.; Mahesh, S.; McCarthy, M. M.; Warby, J. H.; Lin, Y.-H.; Koch, N.; Albrecht, S.; Herz, L. M.; Johnston, M. B.; Neher, D.; Stolterfoht, M.; Snaith, H. J. Understanding and Suppressing Non-Radiative Losses in Methylammonium-Free Wide-Bandgap Perovskite Solar Cells. *Energy Environ. Sci.* **2022**, 15 (2), 714–726.

(30) Jariwala, S.; Burke, S.; Dunfield, S.; Shallcross, R. C.; Taddei, M.; Wang, J.; Eperon, G. E.; Armstrong, N. R.; Berry, J. J.; Ginger, D. S. Reducing Surface Recombination Velocity of Methylammonium-Free Mixed-Cation Mixed-Halide Perovskites via Surface Passivation. *Chem. Mater.* **2021**, 33 (13), 5035–5044.

(31) Khenkin, M. V.; Katz, E. A.; Abate, A.; Bardizza, G.; Berry, J. J.; Brabec, C.; Brunetti, F.; Bulović, V.; Burlingame, Q.; Di Carlo, A.; Cheacharoen, R.; Cheng, Y.-B.; Colsmann, A.; Cros, S.; Domanski, K.; Dusza, M.; Fell, C. J.; Forrest, S. R.; Galagan, Y.; Di Girolamo, D.; Grätzel, M.; Hagfeldt, A.; von Hauff, E.; Hoppe, H.; Kettle, J.; Köbler, H.; Leite, M. S.; Liu, S. (Frank); Loo, Y.-L.; Luther, J. M.; Ma, C.-Q.; Madsen, M.; Manceau, M.; Matheron, M.; McGehee, M.; Meitzner, R.; Nazeeruddin, M. K.; Nogueira, A. F.; Odabaşı, Ç.; Osherov, A.; Park, N.-G.; Reese, M. O.; De Rossi, F.; Saliba, M.; Schubert, U. S.; Snaith, H. J.; Stranks, S. D.; Tress, W.; Troshin, P. A.; Turkovic, V.; Veenstra, S.; Visoly-Fisher, I.; Walsh, A.; Watson, T.; Xie, H.; Yıldırım, R.; Zakeeruddin, S. M.; Zhu, K.; Lira-Cantu, M. Consensus Statement for Stability Assessment and Reporting for Perovskite Photovoltaics Based on ISOS Procedures. *Nat Energy* **2020**, *5* (1), 35–49.

(32) Eperon, G. E.; Paternò, G. M.; Sutton, R. J.; Zampetti, A.; Haghighirad, A. A.; Cacialli, F.; Snaith, H. J. Inorganic Caesium Lead Iodide Perovskite Solar Cells. *J. Mater. Chem. A* **2015**, *3* (39), 19688–19695.

(33) Hu, Y.; Aygüler, M. F.; Petrus, M. L.; Bein, T.; Docampo, P. Impact of Rubidium and Cesium Cations on the Moisture Stability of Multiple-Cation Mixed-Halide Perovskites. *ACS Energy Lett.* **2017**, *2* (10), 2212–2218.

(34) Al-Ashouri, A.; Köhnen, E.; Li, B.; Magomedov, A.; Hempel, H.; Caprioglio, P.; Márquez, J. A.; Morales Vilches, A. B.; Kasparavicius, E.; Smith, J. A.; Phung, N.; Menzel, D.; Grischek, M.; Kegelmann, L.; Skroblin, D.; Gollwitzer, C.; Malinauskas, T.; Jošt, M.; Matič, G.; Rech, B.; Schlatmann, R.; Topič, M.; Korte, L.; Abate, A.; Stannowski, B.; Neher, D.; Stolterfoht, M.; Unold, T.; Getautis, V.; Albrecht, S. Monolithic Perovskite/Silicon Tandem Solar Cell with >29% Efficiency by Enhanced Hole Extraction. *Science* **2020**, *370* (6522), 1300–1309.

(35) Rakocevic, L.; Ernst, F.; Yimga, N. T.; Vashishtha, S.; Aernouts, T.; Heumueller, T.; Brabec, C. J.; Gehlhaar, R.; Poortmans, J. Reliable Performance Comparison of Perovskite Solar Cells Using Optimized Maximum Power Point Tracking. *Solar RRL* **2019**, *3* (2), 1800287.

(36) Bush, K. A.; Frohna, K.; Prasanna, R.; Beal, R. E.; Leijtens, T.; Swifter, S. A.; McGehee, M. D. Compositional Engineering for Efficient Wide Band Gap Perovskites with Improved Stability to Photoinduced Phase Segregation. *ACS Energy Lett.* **2018**, *3* (2), 428–435.

(37) Frohna, K.; Anaya, M.; Macpherson, S.; Sung, J.; Doherty, T. A. S.; Chiang, Y.-H.; Winchester, A. J.; Orr, K. W. P.; Parker, J. E.; Quinn, P. D.; Dani, K. M.; Rao, A.;

Stranks, S. D. Nanoscale Chemical Heterogeneity Dominates the Optoelectronic Response of Alloyed Perovskite Solar Cells. *Nat. Nanotechnol.* **2022**, *17* (2), 190–196.

(38) Tennyson, E. M.; Frohna, K.; Drake, W. K.; Sahli, F.; Chien-Jen Yang, T.; Fu, F.; Werner, J.; Chosy, C.; Bowman, A. R.; Doherty, T. A. S.; Jeangros, Q.; Ballif, C.; Stranks, S. D. Multimodal Microscale Imaging of Textured Perovskite–Silicon Tandem Solar Cells. *ACS Energy Lett.* **2021**, 2293–2304.

(39) El-Hajje, G.; Momblona, C.; Gil-Escrig, L.; Ávila, J.; Guillemot, T.; Guillemoles, J.-F.; Sessolo, M.; Bolink, H. J.; Lombez, L. Quantification of Spatial Inhomogeneity in Perovskite Solar Cells by Hyperspectral Luminescence Imaging. *Energy Environ. Sci.* **2016**, *9* (7), 2286–2294.

(40) Feldmann, S.; Macpherson, S.; Senanayak, S. P.; Abdi-Jalebi, M.; Rivett, J. P. H.; Nan, G.; Tainter, G. D.; Doherty, T. A. S.; Frohna, K.; Ringe, E.; Friend, R. H.; Sirringhaus, H.; Saliba, M.; Beljonne, D.; Stranks, S. D.; Deschler, F. Photodoping through Local Charge Carrier Accumulation in Alloyed Hybrid Perovskites for Highly Efficient Luminescence. *Nat. Photonics* **2020**, *14* (2), 123–128.

(41) Yao, J.; Kirchartz, T.; Vezie, M. S.; Faist, M. A.; Gong, W.; He, Z.; Wu, H.; Troughton, J.; Watson, T.; Bryant, D.; Nelson, J. Quantifying Losses in Open-Circuit Voltage in Solution-Processable Solar Cells. *Phys. Rev. Applied* **2015**, *4* (1), 014020.

(42) Miller, O. D.; Yablonovitch, E.; Kurtz, S. R. Strong Internal and External Luminescence as Solar Cells Approach the Shockley-Queisser Limit. *IEEE J. Photovolt* **2012**, 303–311.

(43) Braly, I. L.; deQuilettes, D. W.; Pazos-Outón, L. M.; Burke, S.; Ziffer, M. E.; Ginger, D. S.; Hillhouse, H. W. Hybrid Perovskite Films Approaching the Radiative Limit with over 90% Photoluminescence Quantum Efficiency. *Nature Photon* **2018**, *12* (6), 355–361.

(44) Stanbery, B. J. Copper Indium Selenides and Related Materials for Photovoltaic Devices. *Critical Reviews in Solid State and Materials Sciences* **2002**, *27* (2), 73–117.

(45) Wilson, G. M.; Al-Jassim, M.; Metzger, W. K.; Glunz, S. W.; Verlinden, P.; Xiong, G.; Mansfield, L. M.; Stanbery, B. J.; Zhu, K.; Yan, Y.; Berry, J. J.; Ptak, A. J.; Dimroth, F.; Kayes, B. M.; Tamboli, A. C.; Peibst, R.; Catchpole, K.; Reese, M. O.; Klinga, C. S.; Denholm, P.; Morjaria, M.; Deceglie, M. G.; Freeman, J. M.; Mikofski, M. A.; Jordan, D. C.; TamizhMani, G.; Sulas-Kern, D. B. The 2020 Photovoltaic Technologies Roadmap. *J. Phys. D: Appl. Phys.* **2020**, *53* (49), 493001.

(46) Barrier, J.; Beal, R. E.; Gold-Parker, A.; Vigil, J. A.; Wolf, E.; Waquier, L.; Weadock, N. J.; Zhang, Z.; Schelhas, L. T.; Nogueira, A. F.; McGehee, M. D.; Toney, M. F. Compositional Heterogeneity in $Cs_{y}FA_{1-y}Pb(Br_{x}I_{1-x})_{3}$ Perovskite Films and Its Impact on Phase Behavior. *Energy Environ. Sci.* **2021**, *14* (12), 6394–6405.

(47) Mundt, L. E.; Zhang, F.; Palmstrom, A. F.; Xu, J.; Tirawat, R.; Kelly, L. L.; Stone, K. H.; Zhu, K.; Berry, J. J.; Toney, M. F.; Schelhas, L. T. Mixing Matters: Nanoscale Heterogeneity and Stability in Metal Halide Perovskite Solar Cells. *ACS Energy Lett.* **2022**, *7* (1), 471–480.

(48) Macpherson, S.; Doherty, T. A. S.; Winchester, A. J.; Kosar, S.; Johnstone, D. N.; Chiang, Y.-H.; Galkowski, K.; Anaya, M.; Frohna, K.; Iqbal, A. N.; Nagane, S.; Roose, B.; Andaji-Garmaroudi, Z.; Orr, K. W. P.; Parker, J. E.; Midgley, P. A.; Dani, K. M.; Stranks, S. D. Local Nanoscale Phase Impurities Are Degradation Sites in Halide Perovskites. *Nature* **2022**, *607* (7918), 294–300.

(49) Bercegol, A.; Ramos, F. J.; Rebai, A.; Guillemot, T.; Puel, J.-B.; Guillemoles, J.-F.; Ory, D.; Rousset, J.; Lombez, L. Spatial Inhomogeneity Analysis of Cesium-Rich Wrinkles in Triple-Cation Perovskite. *J. Phys. Chem. C* **2018**, *122* (41), 23345–23351.

(50) Braunger, S.; Mundt, L. E.; Wolff, C. M.; Mews, M.; Rehermann, C.; Jošt, M.; Tejada, A.; Eisenhauer, D.; Becker, C.; Guerra, J. A.; Unger, E.; Korte, L.; Neher, D.; Schubert, M. C.; Rech, B.; Albrecht, S. $Cs_{x}FA_{1-x}Pb(I_{1-y}Br_{y})_{3}$ Perovskite Compositions: The Appearance of Wrinkled Morphology and Its Impact on Solar Cell Performance. *J. Phys. Chem. C* **2018**, *122* (30), 17123–17135.

(51) Bush, K. A.; Rolston, N.; Gold-Parker, A.; Manzoor, S.; Hausele, J.; Yu, Z. J.; Raiford, J. A.; Cheacharoen, R.; Holman, Z. C.; Toney, M. F.; Dauskardt, R. H.; McGehee, M. D. Controlling Thin-Film Stress and Wrinkling during Perovskite Film Formation. *ACS Energy Lett.* **2018**, *3* (6), 1225–1232.

(52) Kim, S.-G.; Kim, J.-H.; Ramming, P.; Zhong, Y.; Schötz, K.; Kwon, S. J.; Huettner, S.; Panzer, F.; Park, N.-G. How Antisolvent Miscibility Affects Perovskite Film Wrinkling and Photovoltaic Properties. *Nat Commun* **2021**, *12* (1), 1554.

(53) Hu, M.; Bi, C.; Yuan, Y.; Bai, Y.; Huang, J. Stabilized Wide Bandgap MAPbBrxI3–x Perovskite by Enhanced Grain Size and Improved Crystallinity. *Advanced Science* **2016**, *3* (6), 1500301.

(54) Knight, A. J.; Wright, A. D.; Patel, J. B.; McMeekin, D. P.; Snaith, H. J.; Johnston, M. B.; Herz, L. M. Electronic Traps and Phase Segregation in Lead Mixed-Halide Perovskite. *ACS Energy Lett.* **2019**, *4* (1), 75–84.

(55) Gratia, P.; Zimmermann, I.; Schouwink, P.; Yum, J.-H.; Audinot, J.-N.; Sivula, K.; Wirtz, T.; Nazeeruddin, M. K. The Many Faces of Mixed Ion Perovskites: Unraveling and Understanding the Crystallization Process. *ACS Energy Lett.* **2017**, *2* (12), 2686–2693.

(56) Stoumpos, C. C.; Mao, L.; Malliakas, C. D.; Kanatzidis, M. G. Structure–Band Gap Relationships in Hexagonal Polytypes and Low-Dimensional Structures of Hybrid Tin Iodide Perovskites. *Inorg. Chem.* **2017**, *56* (1), 56–73.

(57) Weber, O. J.; Marshall, K. L.; Dyson, L. M.; Weller, M. T. Structural Diversity in Hybrid Organic–Inorganic Lead Iodide Materials. *Acta Crystallographica Section B* **2015**, *71* (6), 668–678.

(58) Seth, C.; Khushalani, D. Non-Perovskite Hybrid Material, Imidazolium Lead Iodide, with Enhanced Stability. *ChemNanoMat* **2019**, *5* (1), 85–91.

(59) Li, Z.; Wang, X.; Wang, Z.; Shao, Z.; Hao, L.; Rao, Y.; Chen, C.; Liu, D.; Zhao, Q.; Sun, X.; Gao, C.; Zhang, B.; Wang, X.; Wang, L.; Cui, G.; Pang, S. Ammonia for Post-Healing of Formamidinium-Based Perovskite Films. *Nat Commun* **2022**, 13 (1), 4417.

(60) Wang, X.; Fan, Y.; Wang, L.; Chen, C.; Li, Z.; Liu, R.; Meng, H.; Shao, Z.; Du, X.; Zhang, H.; Cui, G.; Pang, S. Perovskite Solution Aging: What Happened and How to Inhibit? *Chem* **2020**, *6* (6), 1369–1378.

(61) Ferm, R. J.; Riebsomer, J. L. The Chemistry of the 2-Imidazolines and Imidazolidines. *Chem. Rev.* **1954**, *54* (4), 593–613.